Supporting Information

Carbon Quantum Dot-Modified UiO-66-NH_2 Hybrid Materials: Visible-to-Ultraviolet Upconversion and Enhanced Visible-Light Photocatalysis

Xiangyan Zhong, Xinye He, Ruiqing Long, Linfeng Qi, and Qiang Zhao*

School of Chemical Engineering, Sichuan University, Chengdu 610065, China

***Corresponding author. E-mail**: zhaoqiang@scu.edu.cn

S1. Optimization of the Synthesis Temperature for UiO-66-NH_2

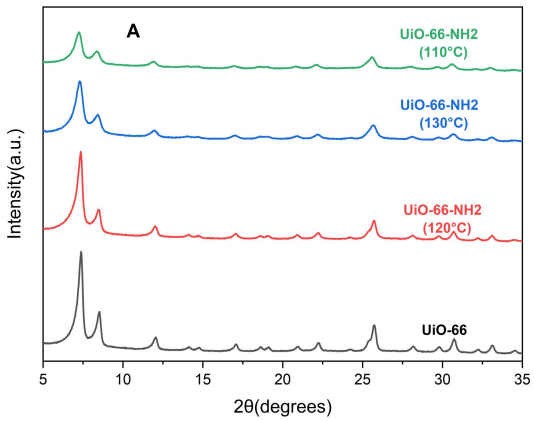

Figure S1. XRD patterns of UiO-66-NH_2 synthesized at different solvothermal temperatures and pristine UiO-66.

The effect of solvothermal temperature on the crystallinity of UiO-66-NH_2 was evaluated by XRD. UiO-66-NH_2 samples synthesized at 110, 120, and 130 °C all retained the characteristic diffraction peaks of the UiO-66 framework, indicating that amino functionalization did not destroy the primary crystalline structure. Among them, the sample prepared at 120 °C exhibited relatively stronger and sharper diffraction peaks, suggesting improved crystallinity under this condition. Therefore, 120 °C was selected as the optimized synthesis temperature for the subsequent preparation of CQDs/UiO-66-NH_2 composites.

S2. Magnified FT-IR Spectra

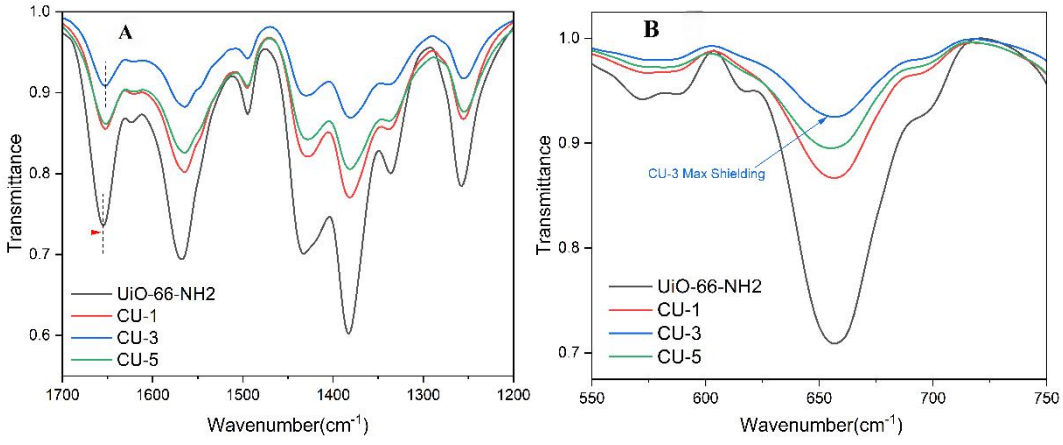

Figure S2. Magnified FT-IR spectra of UiO-66-NH_2, CU-1, CU-3, and CU-5 in the 1700-1200 cm^{-1} region (A) and 550-750 cm^{-1} region (B).

The magnified FT-IR spectra were used to further examine the local chemical environment of the organic linkers and Zr-oxo clusters after CQD incorporation. In the 1700-1200 cm^{-1} region, the

bands associated with amino bending, carboxylate stretching, and aromatic framework vibrations show slight shifts or intensity changes after CQD loading. In the 550-750 cm^{-1} region, the Zr-O-related vibration also changes in intensity, suggesting that CQD incorporation affects the local coordination or interfacial environment of UiO-66-NH_2. These observations support the formation of interfacial interactions between CQDs and UiO-66-NH_2 without disrupting the primary MOF framework.

S3. SEM, SEM-EDS Analysis and TEM

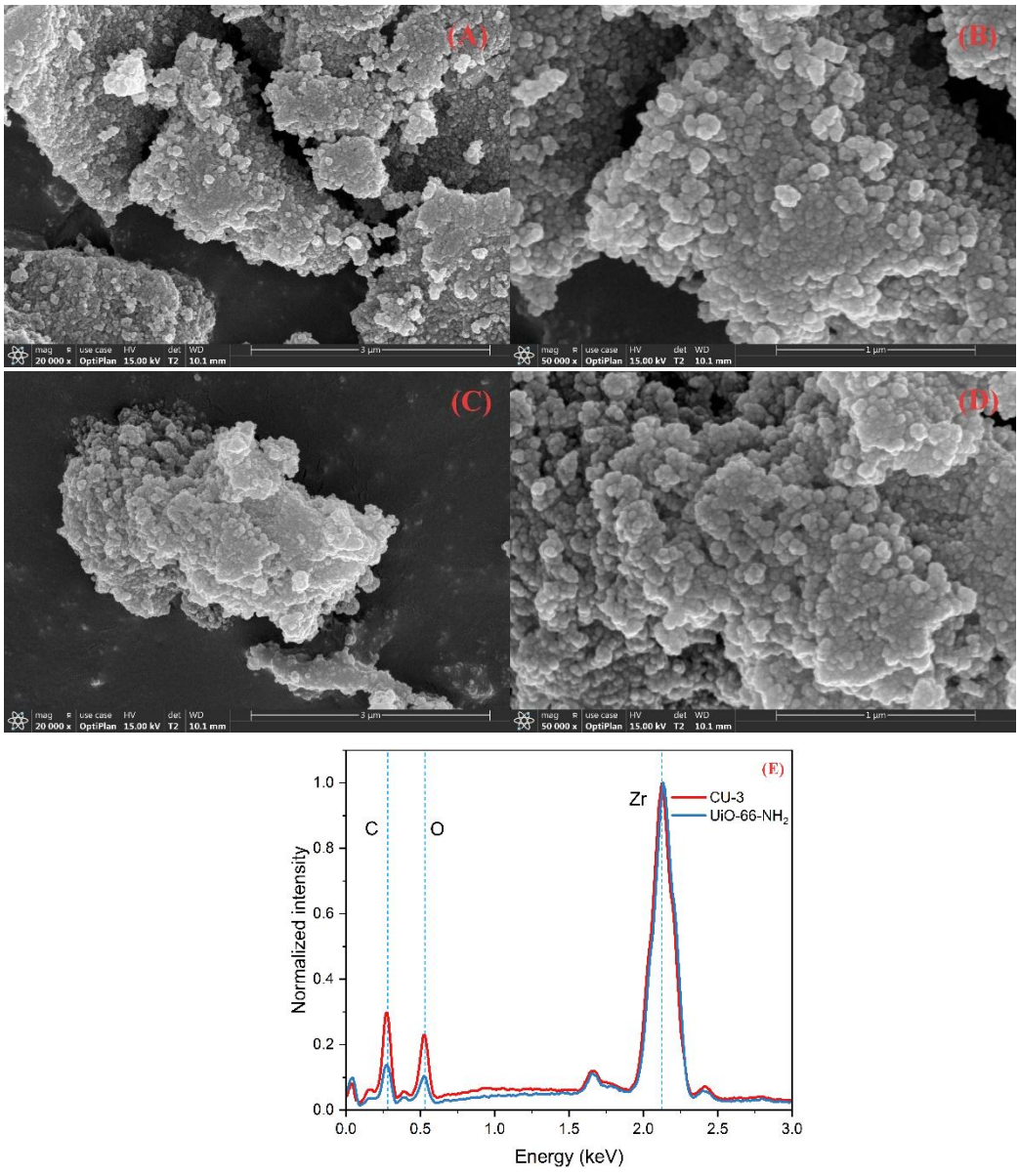

Figure S3. SEM images of UiO-66-NH_2 and CU-3: UiO-66-NH_2 at different magnifications (A,B) and CU-3 at different magnifications (C,D), Zr-normalized SEM-EDS spectra of UiO-66-NH_2 and CU-3(E)

SEM was employed to examine the surface morphologies of UiO-66-NH_2 and CU-3. As shown in **Figure S3A,B**, UiO-66-NH_2 does not display a typical regular octahedral morphology but consists of irregular aggregates formed by the secondary stacking of numerous nanocrystalline particles. The low-magnification image shows micrometer-scale particle aggregates, while the high-magnification image reveals a rough surface composed of densely packed nanoparticles. This morphology may be related to the nucleation and growth process regulated by the acetic acid modulator, the influence of amino-functionalized linkers on crystal growth, and secondary aggregation during drying and sample preparation. Although a regular octahedral morphology is not observed, the distinct characteristic diffraction peaks in the XRD patterns confirm the formation of the UiO-66-NH_2 crystalline framework.

After CQD loading, CU-3 retains a similar stacked nanoparticulate morphology, with no obvious framework collapse or large secondary phases observed in **Figure S3(C,D)**. Compared with pristine UiO-66-NH_2, CU-3 exhibits a rough surface and relatively clear particle boundaries, suggesting that CQD incorporation and the subsequent thermal fixation process do not substantially disrupt the overall microstructure of UiO-66-NH_2. The stacked nanoparticulate morphology of CU-3 may provide interparticle voids and external surface contact regions, which are favorable for pollutant adsorption, light harvesting, and subsequent interfacial charge transfer. Overall, the SEM observations indicate that the composite preserves the main morphological features of UiO-66-NH_2 after CQD incorporation, providing morphological support for the construction of the CQDs/UiO-66-NH_2 composite.

SEM-EDS point spectra were further collected to compare the elemental compositions of UiO-66-NH_2 and CU-3. As shown in **Figure S3E,** both samples exhibit characteristic signals of C, O, and Zr, which are consistent with the organic linkers and Zr-oxo clusters in the UiO-66-NH_2 framework. After normalization to the Zr signal, CU-3 shows relatively enhanced C and O signals compared with pristine UiO-66-NH_2. This result suggests an increased contribution from carbonaceous components and oxygen-containing surface groups after CQD incorporation, which is

consistent with the formation of the CQDs/UiO-66-NH_2 composite. Meanwhile, no obvious additional impurity signals are observed, indicating that the CQD loading process does not introduce detectable inorganic impurities.

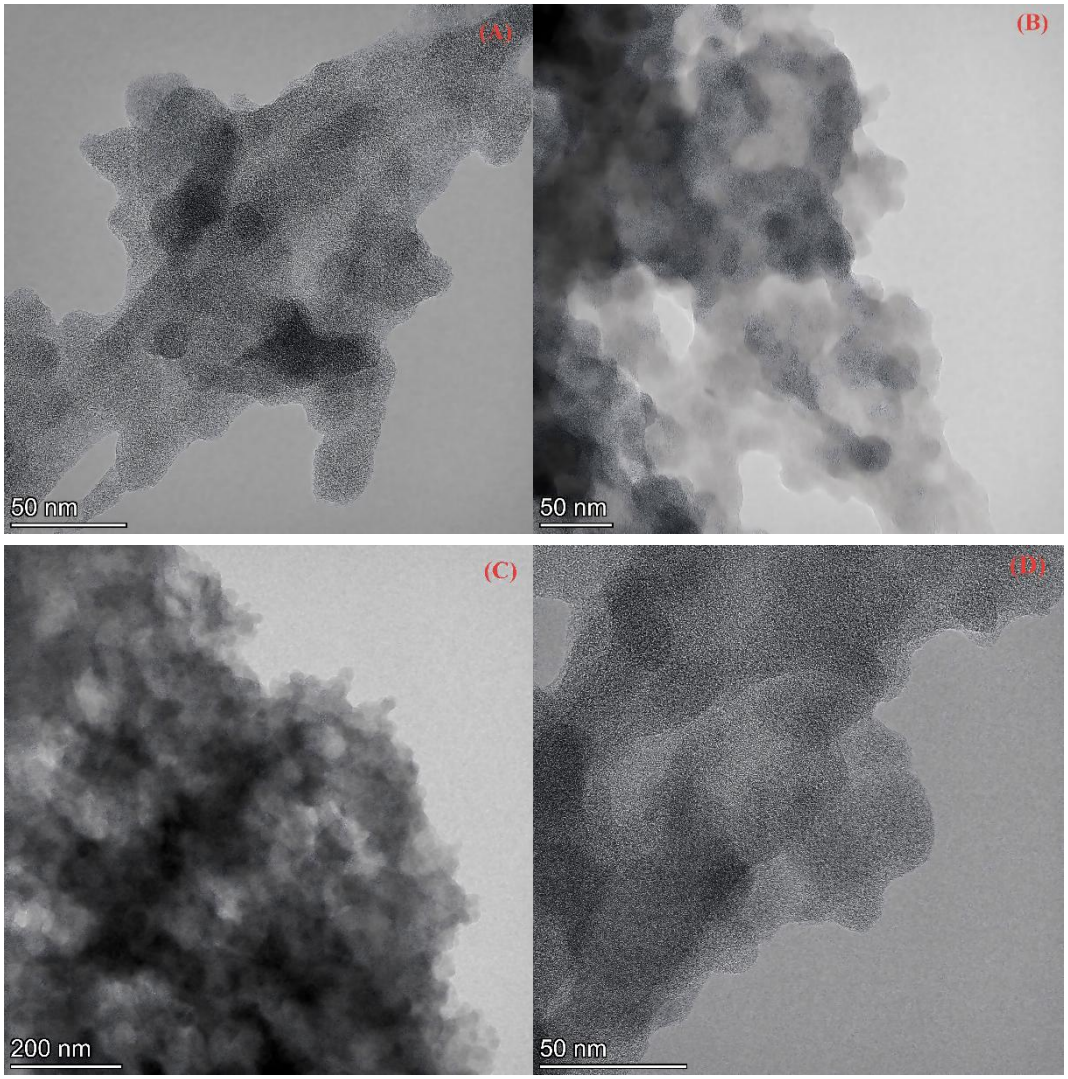

Figure S4. Additional TEM images of UiO-66-NH_2 at different magnifications.

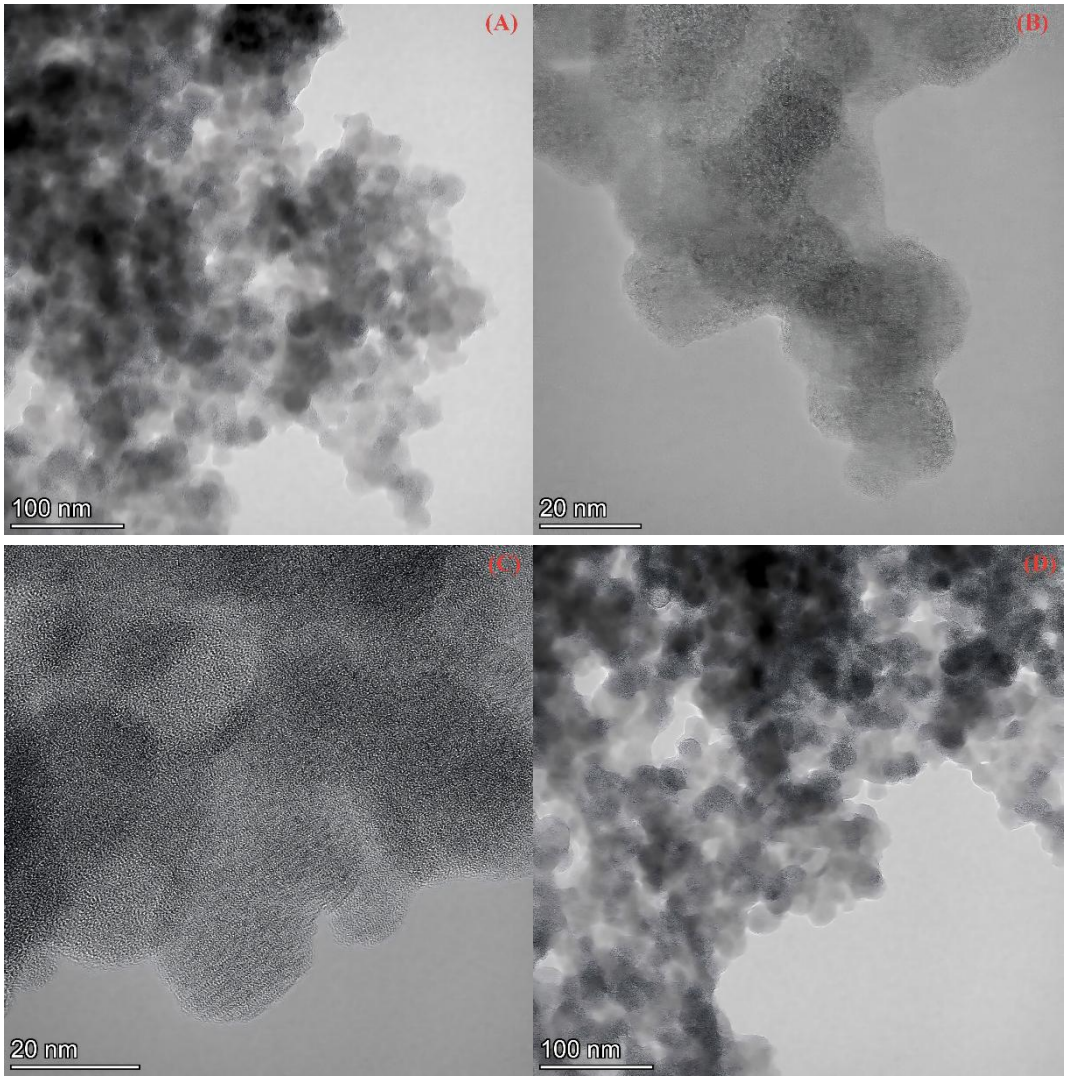

Figure S5. Additional TEM images of CU-3 at different magnifications: (A–D) representative TEM images showing the aggregated nanoparticulate morphology of CU-3

S4. Kinetic Data for the Proof-of-Concept Photocatalytic Reaction

The absorbance values used for the kinetic analysis are summarized in **Table S1**. After dark adsorption equilibrium, the absorbance at the beginning of visible-light irradiation was defined as A_0, and the absorbance values at 30, 60, and 90 min were defined as A_{30}, A_{60}, and A_{90}, respectively. The dark-adsorption stage was not included in the kinetic fitting.

Table S1. Absorbance values used for kinetic analysis.

Sample Groups	A_0	A_{30}	A_{60}	A_{90}
Pristine MOF	0.780	0.719	0.663	0.668
CU-0.5	0.820	0.621	0.576	0.571

Sample Groups	A_0	A_{30}	A_{60}	A_{90}
CU-1	0.881	0.643	0.598	0.592
CU-3	0.870	0.390	0.291	0.288
CU-5	0.924	0.562	0.466	0.451
CU-7	1.061	0.891	0.852	0.851
Pure $FeCl_3$	1.500	1.450	1.390	1.320

These absorbance values were used to calculate $\ln(A_0/A)$ at different irradiation times for pseudo-first-order kinetic analysis.

The pseudo-first-order kinetic parameters were obtained by linear fitting of $\ln(A_0/A)$ versus irradiation time according to Equation: $\ln\left(\frac{C_0}{C}\right) = \ln\left(\frac{A_0}{A}\right) = k_{app}t$ where A_0 is the absorbance at the beginning of visible-light irradiation, A is the absorbance at irradiation time t, and kapp is the apparent rate constant. The calculated $\ln(A_0/A)$ values, apparent rate constants, R^2 values, and relative rates are listed in **Table S2**.

Table S2. Calculated kinetic fitting parameters.

Sample Groups	$Ln(A_0/A_{30})$	$Ln(A_0/A_{60})$	$Ln(A_0/A_{90})$	k_{app}(10-2 min-1)	R^2	Relative Rate (vs Pristine MOF)
Pristine MOF	0.081	0.163	0.155	0.182	0.863	1.000
CU-0.5	0.278	0.353	0.362	0.387	0.780	2.126
CU-1	0.315	0.387	0.398	0.422	0.763	2.317
CU-3	0.802	1.095	1.106	1.203	0.803	6.609
CU-5	0.497	0.685	0.717	0.780	0.832	4.283
CU-7	0.175	0.219	0.221	0.235	0.760	1.294
Pure $FeCl_3$	0.034	0.076	0.128	0.142	0.991	——

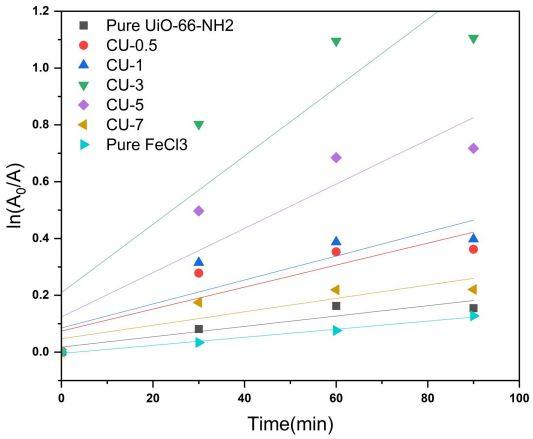

Figure S6. Pseudo-first-order kinetic fitting curves for MO degradation under visible-light irradiation.

As shown in **Figure S6** and **Table S2**, all CQDs/UiO-66-NH_2 composites exhibit higher apparent rate constants than pristine UiO-66-NH_2, confirming that CQD incorporation improves the visible-light photocatalytic degradation kinetics. Among them, CU-3 shows the highest $k_{\_app}$ value of 1.203×10^{-2} min^{-1}, approximately 6.6 times that of pristine UiO-66-NH_2. When the CQD loading is further increased, the kapp values decrease, suggesting that excessive CQDs may cause light shielding, pore occupation, or coverage of active sites.